Biosensors and Bioelectronics 47 (2013) 530–538

Contents lists available at SciVerse ScienceDirect

Biosensors and Bioelectronics

journal homepage: www.elsevier.com/locate/bios

Nickel nanoparticle–chitosan-reduced graphene oxide-modified screen-printed electrodes for enzyme-free glucose sensing in portable microfluidic devices

Jiang Yang [a], Ji-Hyuk Yu [b], J. Rudi Strickler [c], Woo-Jin Chang [b,d,*], Sundaram Gunasekaran [a,*]

[a] Department of Biological Systems Engineering, University of Wisconsin-Madison, 460 Henry Mall, Madison, WI 53706, USA
[b] Department of Mechanical Engineering, University of Wisconsin-Milwaukee, 3200 N. Cramer Street, Milwaukee, WI 53211, USA
[c] Great Lakes Water Institute, University of Wisconsin-Milwaukee, 600 E. Greenfield, Milwaukee, WI 53204, USA
[d] School of Freshwater Sciences, University of Wisconsin-Milwaukee, 600 E. Greenfield, Milwaukee, WI 53204, USA

ARTICLE INFO

Article history:
Received 25 December 2012
Received in revised form
19 March 2013
Accepted 21 March 2013
Available online 3 April 2013

Keywords:
Chitosan
Enzyme-free glucose sensing
Graphene
Nickel nanoparticles
Microfluidic

ABSTRACT

A facile one-step strategy is reported to synthesize nanocomposites of chitosan-reduced graphene oxide–nickel nanoparticles (CS-RGO–NiNPs) onto a screen-printed electrode (SPE). The synthesis is initiated by electrostatic and hydrophobic interactions and formation of self-assembled nanocomposite precursors of negatively charged graphene oxide (GO) and positively charged CS and nickel cations (Ni^{2+}). The intrinsic mechanism of co-depositions from the nanocomposite precursor solution under cathodic potentials is based on simultaneous depositions of CS at high localized pH and *in situ* reduced hydrophobic RGO from GO as well as cathodically reduced metal precursors into nanoparticles. There is no need for any pre- or post-reduction of GO due to the *in situ* electrochemical reduction and the removal of oxygenated functionalities, which lead to an increase in hydrophobicity of RGO and successive deposition on the electrode surface. The as-prepared CS-RGO–NiNPs-modified SPE sensor exhibited outstanding performance for enzymeless glucose (Glc) sensing in alkaline media with high sensitivity (318.4 $\mu A\,mM^{-1}\,cm^{-2}$), wide linear range (up to 9 mM), low detection limit (4.1 μM), acceptable selectivity against common interferents in physiological fluids, and excellent stability. A microfluidic device was fabricated incorporating the SPE sensor for real-time Glc detection in human urine samples; the results obtained were comparable to those obtained using a high-performance liquid chromatography (HPLC) coupled with an electrochemical detector. The excellent sensing performance, operational characteristics, ease of fabrication, and low cost bode well for this electrochemical microfluidic device to be developed as a point-of-care healthcare monitoring unit.

1. Introduction

The risks of renal, retinal, and neural complications are directly associated with Glc levels in body fluids of diabetic patients (Rohlfing et al., 2002). Thus, sensing for Glc in body fluids has been actively pursued, especially based on different electrochemical mechanisms, with (Luo et al., 2010; Luo et al., 2004; Yang et al., 2011a, 2011b) or without (Lu et al., 2009; Mu et al., 2011; Nie et al., 2011; Toghill et al., 2010) using the enzyme glucose oxidase (GO_x). Typically, GO_x catalyzes oxidation of Glc into gluconolactone in the presence of dissolved O_2 (or other 'artificial' electron mediators), with O_2 being reduced to hydrogen peroxide (H_2O_2). Therefore, electrochemical detection of Glc is accomplished by monitoring either O_2 consumption (Yang et al., 2011a) or H_2O_2 production (Luo et al., 2004). With the availability of nanoscale materials, another approach has been developed based on direct electrochemistry of GO_x (Liu et al., 2011). Although GO_x is relatively more stable than other enzymes, use of GO_x-based sensors is limited by relatively high cost, inherent instability, complicated immobilization procedures, and certain critical operational and storage conditions (e.g. temperature, pH, humidity, ionic strength). Therefore GO_x-based Glc sensing is mostly used for real-time monitoring in fermentation processes or *in vivo* human tests, where sterilization is needed (Mu et al., 2011). In contrast, sensors for enzyme-free Glc detection are based on metal (Toghill et al., 2010), metal alloys (Wang et al., 2008) or metal oxides (Mu et al., 2011) as inorganic electrocatalysts using carbon materials such as carbon nanotubes (CNTs) and graphene as scaffolds (Nie et al., 2011). For example, an electrodeposited PdNi- and Pd-coated screen-printed carbon electrodes are reported for Glc oxidation at a low overpotential under alkaline conditions (Huang and Chen, 2010). These enzyme-free

* Corresponding authors.
E-mail addresses: wjchang@uwm.edu (W.-J. Chang).
guna@wisc.edu (S. Gunasekaran).

0956-5663/$ - see front matter © 2013 Elsevier B.V. All rights reserved.
http://dx.doi.org/10.1016/j.bios.2013.03.051

sensors, despite the need for most of them to be operated in alkaline conditions, perform better than the enzyme-based sensors and exhibit improved sensitivity, stability, response time, and detection limit; in addition, they are also less expensive (Mu et al., 2011). Many researchers have reported superior sensing performance of enzyme-free Ni-based (i.e., Ni, NiO, $Ni(OH)_2$) sensors due to the formation of strong oxidizing NiO(OH) in alkaline conditions (Ai et al., 2008; Lu et al., 2009; Mu et al., 2011); Ni is also abundantly available, making it an inexpensive electrocatalyst for Glc sensing.

Chitosan (CS) is a linear amino polysaccharide derived from partial deacetylation of chitin. It is a nontoxic cationic biopolymer, and exhibits good biocompatibility, biodegradability, adhesiveness, and film-forming ability (Yang et al., 2010); it can also serve as antifouling protective coating (Bulwan et al., 2009). CS has been extensively used as an integrative biomaterials and immobilization matrices to assist in the fabrication of sensors and lab-on-a-chip devices. CS films can be easily prepared by drop-casting (Han et al., 2010), spin-coating (Jawaheer et al., 2003), electrodeposition (Wu et al., 2005), and nano-imprinting (Park et al., 2007). Among these approaches, electrodeposition, which takes advantage of the pH-dependent solubility of the material (Wu et al., 2005), is the most controllable. CS is well-known to electrodeposit in response to high localized pH values (>5.0) at cathode surface and has been widely used to mediate co-depositions of nanoparticles (NPs), enzymes, and carbon materials. Zeng et al. fabricated an enzymatic Glc sensor by co-electrodepositing CS-IL-GO_x–AuNPs via a two-step approach (Zeng et al., 2009). Yang et al. constructed a nitrite sensor by one-step electrodeposition of CS-CNTs–CuNPs nanocomposite under constant cathodic potential (Yang et al., 2010). Wan et al. described an impedimetric immunosensor for label-free bacteria detection by controllable electrodeposition of CS and RGO (Wan et al., 2011); however, this approach requires complicated fabrication procedures, because RGO is reduced by hydrazine prior to deposition.

Graphene obtained from GO is readily and inexpensively available (Segal, 2009). Electrochemical reduction of GO is simple, rapid, green, and effective (Yang et al., 2011a), and it prevents the use of any toxic or corrosive reducing reagents or stabilizers that might damage its electronic properties. The almost insulating GO becomes highly conductive RGO when the undesired oxygen species are eliminated by electrochemical reduction (Yang et al., 2011a) or other effective deoxygenating process (Pei et al., 2010). It has been reported that GO, along with AuNPs, can be directly electrodeposited onto electrode surface and electrochemically reduced *in situ* owing to the different solubilities of GO and RGO (Liu et al., 2011). Since GO, CS, and metal NPs (e.g., NiNPs) can be electrodeposited at pH 5 under cathodic potentials and they can form nanocomposite precursors by electrostatic and hydrophobic interactions (Scheme 1), the nanocomposites can be synthesized directly on the electrode surface. There are three roles of GO in this study: it helps to form the self-assembled precursor nancomposite as a scaffold; its reduced form RGO endows hydrophobicity for deposition from the aqueous solution; RGO also provides much fast electron transfer capability for redox reactions.

The motivation for this study is to fabricate an inexpensive and enzyme-free miniaturized lab-on-chip device for routine Glc measurement by end users. Therefore, in our design we sought to combine the high sensitivity, rapidity, simplicity, and low detection limit advantages of electrochemical sensing; small sample volume, easy manual sample injection, and miniaturization advantages of microfluidics; and low cost and replaceability advantages of screen-printed electrodes (SPEs). Few similar investigations include that of Joo et al., who reported an enzyme-free electrochemical Glc sensing using nanoporous Pt in a microfluidic system driven by electro-osmotic flow (Joo et al., 2007) and that of Vlandas et al., who fabricated a single-wall carbon nanotube sensor in microfluidic channels for enzyme-free sensing of sugar (Vlandas et al., 2010).

Herein we describe the development of a portable electrochemical microfluidic system housing commercial SPEs for real-time measurement of Glc. The SPEs were modified by a simple CS-mediated one-step co-electrodeposition of self-assembled CS, GO and NiNPs nanocomposite precursors at pH 5, while GO (Yang et al.,

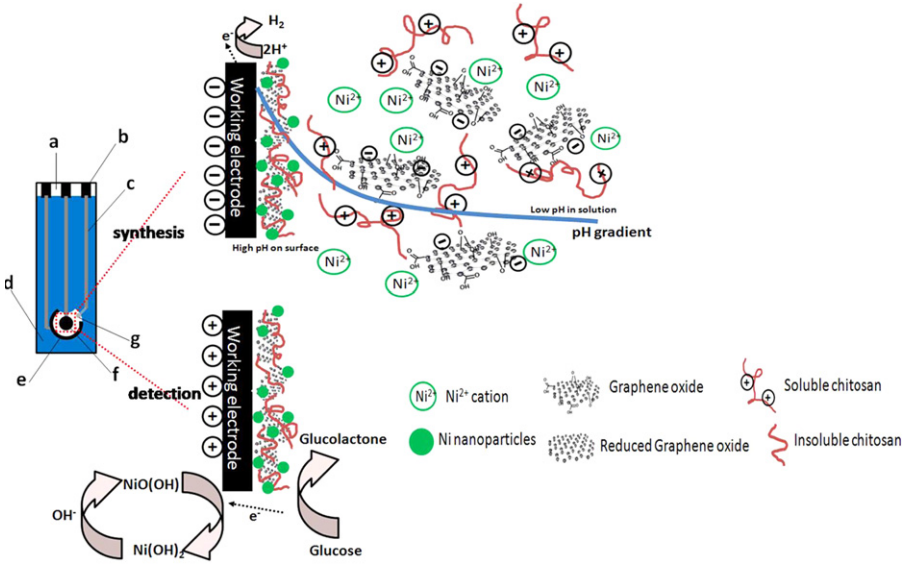

Scheme 1. Schematic diagram of the electrodeposition processes of CS-RGO–NiNPs on SPE surface and its Glc detection mechanism. (a) polypropylene, (b) carbon electrical contacts, (c) conductive paths, (d) Insulting dielectric, (e) carbon counter electrode, (f) carbon working electrode, (g) Ag/AgCl pellet reference electrode. Synthesis (upper part of the figure): the synthesis reaction begins with the formation of nanocomposite precursors by electrostatic and hydrophobic interactions between negatively charged GO and positively charged Ni^{2+} and CS chains. With cathodic potential applied, protons in the acid solution around the electrode surface are consumed, causing relatively high localized pH. As a result, CS chains in the nanocomposite precursors near the electrode become insoluble and deposited from bulk solution together with GO and Ni^{2+}. On the electrode surface, GO and Ni^{2+} are *in situ* reduced into RGO and NiNPs and deposited simultaneously with the deposition of CS. Detection (lower part of the figure): the detection reaction under applied anodic constant potentials starts with oxidation of Ni(0) into Ni(II) species such as $Ni(OH)_2$ and NiO. These Ni(II) species are then further oxidized into strongly oxidizing Ni(III) species as NiO(OH) which electrochemically catalyzes the oxidation of glucose into gluconolactone liberating two hydrogen atoms. Meanwhile, NiO(OH) itself is reduced back into Ni(II) species.

2011a) was electrochemically reduced *in situ* upon deposition without requiring pre- or post-reductions. The electrodeposition and reduction reactions of both GO and Ni precursor occurred simultaneously (Liu et al., 2011) with CS deposition. The resulting CS-RGO–NiNPs nanocomposite facilitated electron transfers and endowed high electrocatalytic activity for non-enzymatic Glc sensing. The as-fabricated sensor exhibited high sensitivity, good stability and selectivity towards Glc, with a wide linear range covering Glc levels in physiological fluids of normal individuals. Therefore, it has the potential to be further developed into a pocket-sized, enzyme-free, point-of-care analytical device for routine Glc monitoring.

2. Materials and methods

2.1. Chemicals and reagents

Graphite powder and D(+)-glucose anhydrous were purchased from Sinopharm Chemical Reagent Co., dopamine hydrochloride (DA), uric acid (UA) and L-ascorbic acid (AA) were purchased from Acros Organics and nickel (II) sulfate hexahydrate ($NiSO_4$•$6H_2O$) was obtained from Alfa Aesar. High molecular weight CS (from crab shells) was purchased from Sigma-Aldrich Chemicals. All other reagents were of analytical grade and used as received without further purification. Doubly distilled Milli-Q water (ddH_2O) (>18.2 MΩ) was used for all experiments and high purity N_2 was used for deaeration where needed. SPEs were purchased from Zensor featuring graphitic carbon working (with geometric area of ~ 7.07 mm^2) and counter electrodes and Ag/AgCl pellet reference electrode (Scheme 1). 0.1 M NaOH was used as the supporting electrolyte for Glc detection throughout, unless otherwise stated.

2.2. Instrumentation

Scanning electron microscopy (SEM) and energy dispersive X-ray spectroscopy (EDS) were conducted using EDS-integrated LEO 1530 Gemini FESEM (Carl Zeiss, USA) for characterizing surface morphology and elemental composition of the sample. Particle size distribution was determined using Image-Pro Plus software. Attenuated total reflectance-Fourier transform infrared spectroscopy (ATR-FTIR) was conducted with PerkinElmer Spectrum 100 (PerkinElmer, MA, USA). Cyclic voltammetry (CV), chronoamperometry and electrochemical impedance spectroscopy (EIS) were performed on a CHI 660D Electrochemical Analyzer (CH Instruments, TX, USA) at ambient temperature (25 ± 1 °C) using three-electrode configuration. EIS was carried out in a solution containing 0.01/0.01 M $[Fe(CN)_6]^{4-/3-}$ and 1.0 M KCl supporting electrolyte in the frequency range of 0.1–10^5 Hz. HPLC analysis was performed using Dionex ICS-3000 HPLC system (Dionex Corporation, MA, USA) equipped with Carbopac™ PA1 guard column at 20 °C and an electrochemical detector using Au, Ti, and pH-Ag/AgCl as working, counter, and reference electrodes, respectively. Eluent was supplied at a rate of 0.7 mL min^{-1} as follows: water for 25 min, water plus 0.1 M NaOH at 3:7 (v/v) for 10 min, followed by water for 10 min. To achieve stable baseline and better sensitivity, 0.5 M NaOH was used at 0.3 mL•min^{-1} as post-column eluent. Glc was eluted starting at around 5.6–5.8 min, with the retention peak centered at around 6.0–6.5 min varying by standards and samples. Glc concentrations from HPLC-amperometry were calculated by integrating the area under designated peaks and standard calibration curves. Error bars indicate triplicate measurements unless otherwise noted.

2.3. Fabrication of CS-RGO–NiNPs-modified working electrodes

Well-exfoliated GO was synthesized via modified Hummer's method (Yang et al., 2011a, 2012). Concentrated H_2SO_4 and $KMnO_4$ were used to obtain pre-oxidized graphite, which was then re-oxidized to GO by H_2O_2. After sonication, delamination of GO sheets were achieved and stable exfoliated GO aqueous dispersion can be obtained due to negative electrostatic repulsion from ionization of carboxyl and phenolic hydroxyl groups on GO sheets (Liu et al., 2011). CS solution was prepared by adding CS platelets to water and gradually adjusting the pH to ~3.0 with HCl (Luo et al., 2004; Wu et al., 2005). The solution was vortexed for 10 min and sonicated for 30 min, before it was filtered to remove any insoluble contents with pH adjusted to 5.0 using NaOH. GO and $NiSO_4$ were added to have final concentrations of 1 mg mL^{-1} GO, 3 mM $NiSO_4$ and 0.4% CS with final pH value maintained at 5.0. After being mixed under stirring for 1 h at room temperature, the solution was further sonicated to be homogenous and stable and was then deaerated by purging N_2 for 15 min. For electrodeposition, SPE was immersed in the above suspension horizontally and multiple cathodic CV cycling was conducted in the potential range from 0.0 V to −1.5 V at a scan rate of 50 mV s^{-1} for 40 cycles. After deposition, the CS-RGO–NiNPs modified SPE was gently rinsed with water and dried at room temperature. RGO- and CS-RGO modified SPEs were also prepared similarly using corresponding deposition solutions for comparison. Before any Glc measurement, CS-RGO–NiNPs modified SPEs were pretreated in 0.1 M NaOH by 40 consecutive CV cycles from 0.0 V to +0.8 V at 0.1 V s^{-1} to reach the steady state until almost no obvious change in peak current (Fig. S1). This pretreatment has been widely used to facilitate the formation of Ni oxyhydroxide for stable Ni-based enzyme-free Glc sensing (Lu et al., 2009; Nie et al., 2011). Fresh deposition solution was prepared for every 2–3 electrodes, and pH was maintained at 5.0 prior to each deposition. Electrodes were stored in a Petri dish at room temperature when not in use.

2.4. Fabrication of the portable microfluidic device with replaceable SPEs

The mold for PDMS chamber and the device holder were prepared using acrylonitrile butadiene styrene (ABS) plastic. A 10:1 mixture of Sylgard 184 (Dow Corning Co.) was poured on top of the mold and peeled off after curing for three days at room temperature. Two holes were drilled in the PDMS chamber to accept inlet and outlet tubes (760 μm OD, 250 μm ID, Cole-Parmer Co.). The detailed device setup is shown in Scheme 2. The PDMS chamber was placed on top of the sensor and fixed by the ABS holder. The microfluidic chamber embedded in PDMS chamber was carefully aligned with the active area on the modified SPE sensor. One of the two holders has square or circular shape through the hole so that the inlet and outlet tubes can be connected to the PDMS chamber. The whole device stack was firmly held by Quick Grip® Micro Bar Clamp and Spreader (American Tool Inc.) to prevent any possible leaking from the chamber. The inlet tube was connected to a 10-mL microsyringe for sample injection; the inlet tube can also be connected to a pump, micropipettor or dropper, as needed. Samples could be injected manually at a slow and steady rate or by an adjustable syringe pump. Based on the dimensions of the PDMS chamber (7 mm diameter, 0.2 mm height), the calculated sample volume required for detection using this device is 7.7 μL. After measurements, the used SPE can be easily removed and replaced with a fresh one.

3. Results and discussion

3.1. Characterizations of CS-RGO–NiNPs

SEM image of unmodified and CS-RGO–NiNPs modified SPEs are shown in Fig. S3 and Fig. 1a, respectively. The pristine carbon SPE showed a typical graphite structure with highly dispersed carbon particles observed blurred and irregular shapes and there

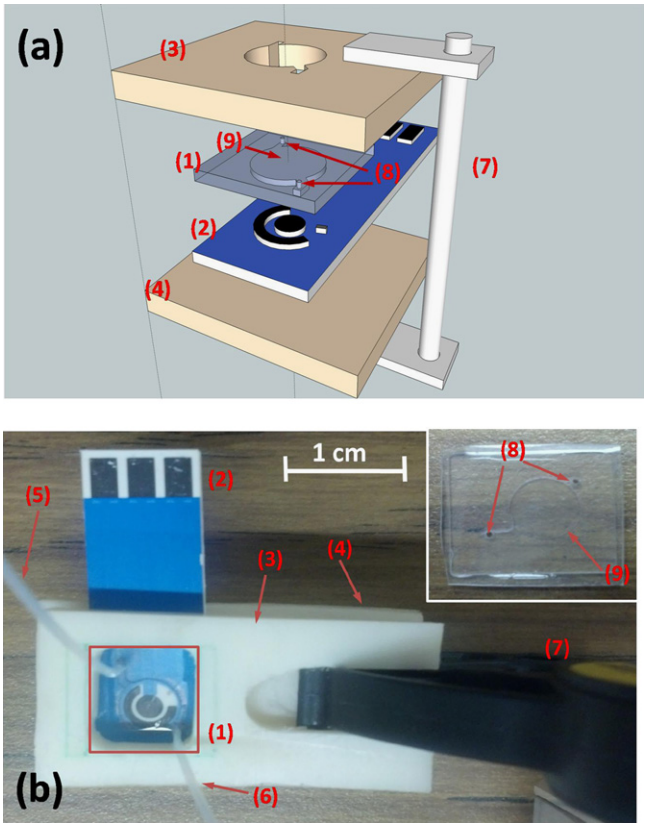

Scheme 2. (a) Schematic of the device stack setup. **(b)** Photograph of the as-fabricated microfluidic electrochemical device for sensing Glc. (1) PDMS chamber (inset in (b) shows an enlarged view) (2) CS-RGO–NiNPs modified SPE (3) top piece of plastic device holder (4) bottom piece of plastic device holder (5) outlet tubing (6) inlet tubing connected to a sample injector (syringe or pump) (7) Micro bar clamp/spreader (8) holes for connecting inlet and outlet tubes (9) circular chamber fit to the sensing area.

are no obvious wrinkled structures or NPs observed (Fig. S3). As for CS-RGO–NiNPs, a rough webbed surface with flake-like graphite sheet particles can be observed with many exposed edge-plane sites/defects, which usually serve as origins of electron transfers at the electrode (Kadara et al., 2009). Fairly dense network of NiNPs had been homogenously deposited onto the pristine graphite sheets. The NPs are mostly spherical and fairly uniform in size (31.7 ± 4.7 nm) (Fig. 1b), and tended to be clustered and interconnected throughout the electrode surface. CS chains play a vital part in the growth and assembly of clusters of NPs, which are entrapped in CS network or coated with CS (Potara et al., 2012). Typical wrinkled graphene sheet structure can be clearly seen, indicating the presence of flexible and thin graphene sheets (Fig. 1a).

A possible deposition process of CS-RGO–NiNPs nanocomposites is assumed as follows. In the deposition solution, positively charged CS and Ni^{2+} cations interact by chelating (Adewuyi et al., 2011), while negatively charged GO sheets can form composites with both CS and Ni^{2+} via electrostatic interactions in the solution. Hydrophobic moieties in CS such as acetyl groups and glucosidic rings might interact with the hydrophobic part of GO basal planes via partially hydrophobic interactions. As a result, self-assembled conjugates of CS-GO–Ni^{2+} are formed. With applied cathodic potentials leading to electrode polarization, the proton in the acidic solution around the electrode surface is consumed and local pH is increased, forming a localized pH gradient from the electrode surface (Wu et al. 2005). CS chains in the nanocomposite precursors near electrode surface become insoluble due to higher pH, whereas CS chains in the bulk solution (pH 5.0) remain soluble (Scheme 1). Therefore, as CS chains are deposited onto the electrode surface, GO sheets and NiNPs are co-deposited into CS matrices at the same time. Moreover, GO sheets (Liu et al., 2011) and NiNPs (Toghill et al., 2010) might also be deposited at cathodic potentials under these conditions. With continued cathodic potential sweeping, GO sheets are electrochemically reduced *in situ* efficiently and Ni cations are simultaneously reduced, with NPs nucleated and entrapped in CS as clusters. The reduction product RGO becomes more hydrophobic than GO because oxygen species are eliminated, and thus gets deposited onto the electrode surface. The nanocomposites then form and progressively link together, and RGO with improved properties for electron transfers affords effective nucleation sites for NiNPs enhancing the electrodeposition.

NiNPs are formed owing to the highly supersaturated solution of anionic species (SO_4^{2-}, GO, Cl^-), well-controlled production on time scale (i.e., potential sweeping range, scan rate and cycles) and possibly the existence of hydrogen evolution under low pH which leads to the formation of NPs without faceted morphology (Nasirpouri et al., 2011). The assumptions are further supported by the voltammetric behaviors during the synthesis in stable dispersions (Fig. S2). A typical crossing of CV curve (loop) can be seen in the reverse scan, representing the characteristics of electrodeposition processes of Ni and carbon materials (Martis et al., 2010). As the synthesis progresses, the cathodic current intensity decreased from the 1st to the 13th cycle and H^+ is reduced and thus CS is deposited leading to reduced conductivity. During this process, NiNPs are yet completely nucleated and decrease in cathodic current might be also attributed to successful *in situ* electrochemical reduction of GO, as we reported previously (Yang et al., 2012). However, the current surprisingly increased from the 14th cycle onwards, which is primarily associated with the synthesis of NiNPs. Elemental composition of CS-RGO–NiNPs was analyzed by simultaneous EDS (Fig. 1c). Strong signature peaks of C, O, and Ni were observed, along with a weak peak indicating N. Carbon came from both the substrate and electrochemically deposited and reduced GO sheets. Oxygen species originated from the substrate, deposited CS, electrochemically unreduced oxygen species on RGO (Yang et al., 2012), and possibly oxide or hydroxide Ni species during deposition (Toghill et al., 2010). The presence of 1.2 and 8.5 atomic percentages of N and Ni, respectively manifested the successful electrochemical deposition of CS and NiNPs.

ATR-FTIR transmittance spectra of pristine CS, GO, and CS-RGO are shown in Fig. 1d. As seen in CS (curve 1), the characteristic peaks of the following CS functionalities are observed: a broad and intense band (3300–3450 cm^{-1}) centered around 3350 cm^{-1} from N–H stretching vibrations in amide or amine groups and overlapped O–H stretching vibration in hydroxyl group (Wei and Qian, 2008); both methyl characteristic bands at 2910 and 2880 cm^{-1} from strong and moderate C–H stretching vibration in acetylated CS; three characteristic amide bands at 1653 $cm^{-1}$from C=O stretching vibration (chitin residues), 1591 cm^{-1} from N–H deformation vibration in amine group, 1423 cm^{-1} from C–H deformation vibration; bands of saccharine structures at 1377 cm^{-1} from C–OH stretching vibration, 1150, 1080 and 1030 cm^{-1} from symmetric and asymmetric C–O stretching vibrations in ether or ester groups. These results are similar to those in literature (Han et al., 2010; Wan et al., 2011; Wei and Qian, 2008). The spectrum of GO manifested a number of oxygen functionalities, as we have reported previously (Yang et al., 2012): a broad and strong band at 3400 cm^{-1} from O–H stretching vibration in intercalated water, an overlapped broad band at 3200 cm^{-1} of O–H coupling stretching vibration in carboxyl group, a sharp peak at 1732 cm^{-1} from C=O stretching vibration in carbonyl group, C=C band at

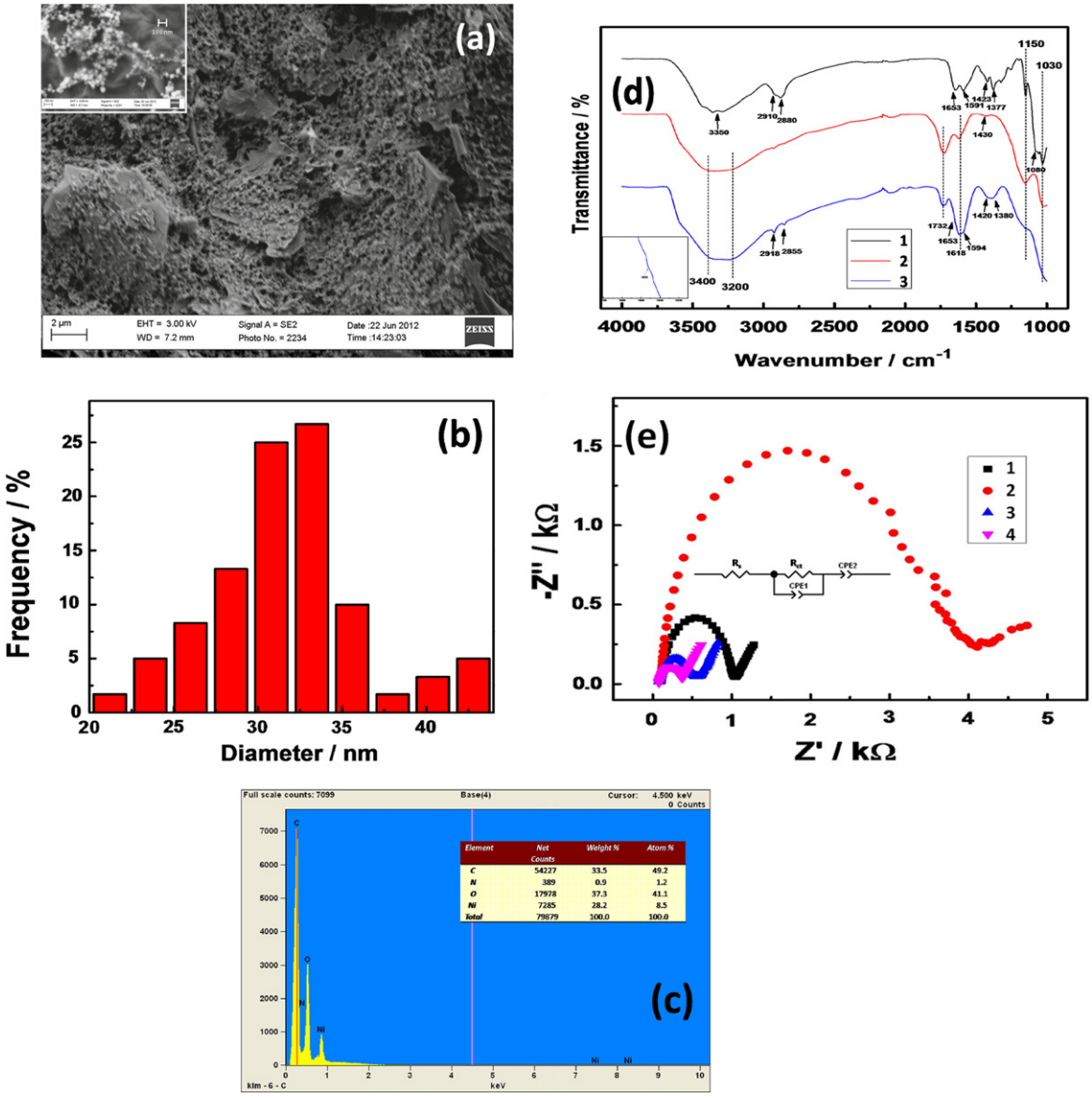

Fig. 1. (a) SEM images of CS-RGO–NiNPs electrode. Inset shows higher magnification. (b) Particle size distribution of NiNPs. (c) EDS spectra of CS-RGO–NiNPs. Inset shows corresponding quantitative analyses. (d) ATR-FTIR spectra of pristine CS (1), GO (2) and electrodeposited CS-RGO (3). Inset shows magnification of weak band of (3) at 1653 cm^{-1}. (e) EIS of bare (1), CS (2), CS-RGO (3) and CS-RGO–NiNPs (4) modified SPEs. Inset shows the equivalent circuit for CS-RGO–NiNPs modified SPEs. R_s: solutions resistance; R_{ct}: charge transfer resistance; CPE: constant phase element.

1620 cm^{-1} from skeletal vibrations of unoxidized graphitic domains, a weak broad band at 1430 cm^{-1} from O–H deformation vibration in carboxyl group, a strong band at 1150 cm^{-1} from C–O stretching in ether or ester groups and a shoulder band at 1030 cm^{-1} of C–O stretching vibration in epoxy or alkoxy groups. In the electrodeposited CS-RGO, the large broad band of N–H and partially overlapped O–H stretching from 3200-3450 cm^{-1} remains and unreduced oxygen species in GO might also contribute to this band (Chen et al., 2011). Dramatically weaker and shifted methyl peaks are still present at 2918 and 2855 cm^{-1} due to hydrolysis of acetyl groups during electrodeposition (Wan et al., 2011). A very weak band (see inset) at 1653 cm^{-1} and slightly shifted bands at 1594 cm^{-1}, 1420 and 1380 $cm^{-1}$are indicative of amide groups from CS. The band shifts might be attributed to chemical bonding between CS and RGO, such as hydrogen bonding or interactions of active groups such as carboxyl, hydroxyl and amine groups (Wan et al., 2011). Meanwhile, the intensities of C=O stretching vibration at 1732 cm^{-1} and C–O stretching vibration at 1150 and 1030 cm^{-1} decreased drastically whereas the intensity of C=C skeletal vibration band at 1620 cm^{-1} in CS-RGO is much stronger than GO, demonstrating successful electrochemical reduction and RGO has high purity. These results suggest that CS and GO have been successfully synthesized on the electrode surface by co-deposition and GO has been electrochemically reduced *in situ*.

EIS is useful to study the electron transfer characteristics in the electrode–electrolyte interface and to track electrode surface modifications as presented in Nyquist complex-plane plots of differently-modified electrodes in the presence of equimolar $[Fe(CN)_6]^{4-/3-}$ redox probes (Fig. 1e). The equivalent circuit model (Fig. 1e inset) is comprised of the series of solution resistance (R_s), the parallel combination of Faradic charge transfer resistance (R_{ct}) and a constant phase element (CPE), and another CPE. The fitting result with experimental data is shown in Fig. S4. CPE is defined as CPE-T and CPE-P. When CPE-P is close to 0, CPE can be regarded as an ideal resistor; when CPE-P is close to 1, it represents an ideal capacitor; when CPE is close to 0.5, CPE is associated with the diffusion process and termed as Warburg impedance. CPE is used

instead of a pure capacitor/resistor to compensate for non-ideal conditions at the interface, reflecting the inhomogeneity and defects on the surface (Maalouf et al. 2007). The fitted values for each element are listed in Table S1. CPE1 in this study acts more like a capacitor whereas CPE2 can be considered for Warburg diffusion. In the meantime, compared to the unmodified electrode (curve 1, R_{ct}=900 Ω), the electrode modified by CS deposition yielded a much larger semicircle (curve 2, R_{ct}=3447 Ω) implying large resistance to the redox probe in the electrolyte solution. This might be ascribed to the diffusion of redox probes and interfacial electron transfers towards electrode surface that are hindered by CS. CS-RGO modified electrode (curve 3) has a significantly smaller R_{ct} (416 Ω) than the CS-modified electrode, due to greatly enhanced electron transfers within RGO interpenetrating network (Yang et al., 2011a). The unreduced GO behaves nearly as an insulator and prohibited electrochemical properties owing to the presence of excessive oxygen species (Chen et al., 2011), here it confirms successful *in situ* elimination of electrochemically unstable oxygen species during deposition, which facilitates electron transfers. This result is also well-supported by the gradually decreasing cathodic current in CV profiles during initial deposition (Fig. S2), similar to those previously reported (Liu et al., 2011; Yang et al., 2011a). R_{ct} of CS-RGO–NiNPs (273 Ω) further decreased with modification of Ni metal NPs, suggesting NiNPs are beneficial for electron transfers by providing favorable conduction pathways or probably by synergistic effects in the nanocomposites. Therefore, CS-RGO–NiNPs can dramatically improve the electron transfer efficiency at the electrolyte–electrode surface.

3.2. Electrochemical properties and electrocatalytic activities towards Glc at CS-RGO–NiNPs

The electrocatalytic activity of CS-RGO–NiNPs towards Glc was studied by CV in 0.1 M NaOH (Fig. 2a). In the absence of Glc, both bare (curve 3) and CS-RGO modified (curve 5) electrodes displayed a rather broad and unobvious anodic peak around +0.45 V (Fig. 2a inset and magnification in Fig. S5) which might come from electrochemical behavior of quinone/hydroquinone groups typically present in carbon material. After the addition of 5 mM Glc, there was only a negligible increase in current at the bare electrode (curve 4) while at CS-RGO electrode, rather than an increase, a tiny decrease in current was surprisingly observed (curve 6), possibly caused by electrochemical reduction of the remaining unreduced GO. In contrast, a pair of well-defined redox peaks appeared at CS-RGO–NiNPs electrode in the absence of Glc, with the cathodic and anodic peaks at +0.35 V and +0.50 V respectively corresponding to Ni(III)/(II) redox couple as described in the literature (Lu et al., 2009; Nie et al., 2011). This typical nonsymmetrical face wave of Ni in 0.1 M NaOH is associated with the irreversible process of oxidation–reduction (Zhao et al., 2007). Ni(0) is firstly oxidized into Ni(II) to form predominantly $Ni(OH)_2$ (Eq. (1)) at potential less than −600 mV (also possibly along with NiO (Lu et al., 2009; Luo et al., 1996)) and Ni(II)species are further oxidized into Ni(III) as NiO(OH) (Eq. (2)), as described below (Lu et al., 2009; Nie et al., 2011; Zhao et al., 2007)

$$Ni + 2OH^- - 2e^- \leftrightarrow Ni(OH)_2 \quad (1)$$

$$Ni(OH)_2 + OH^- - e^- \leftrightarrow NiO(OH) + H_2O \quad (2)$$

Upon adding 3 mM Glc, anodic peak current increased and cathodic current decreased, suggesting the CS-RGO–NiNPs can mediate Glc oxidation. Considering the poor electrocatalytic activities of CS-RGO and bare electrodes against Glc, NiNPs in the nanocomposites are responsible as an enzyme mimicking catalyst for Glc oxidation with a possible mechanism directed by Ni(III) with two hydrogen liberated (Scheme 1), as below (Eq. (3)) (Lu et al., 2009; Nie et al., 2011; Zhao et al., 2007)

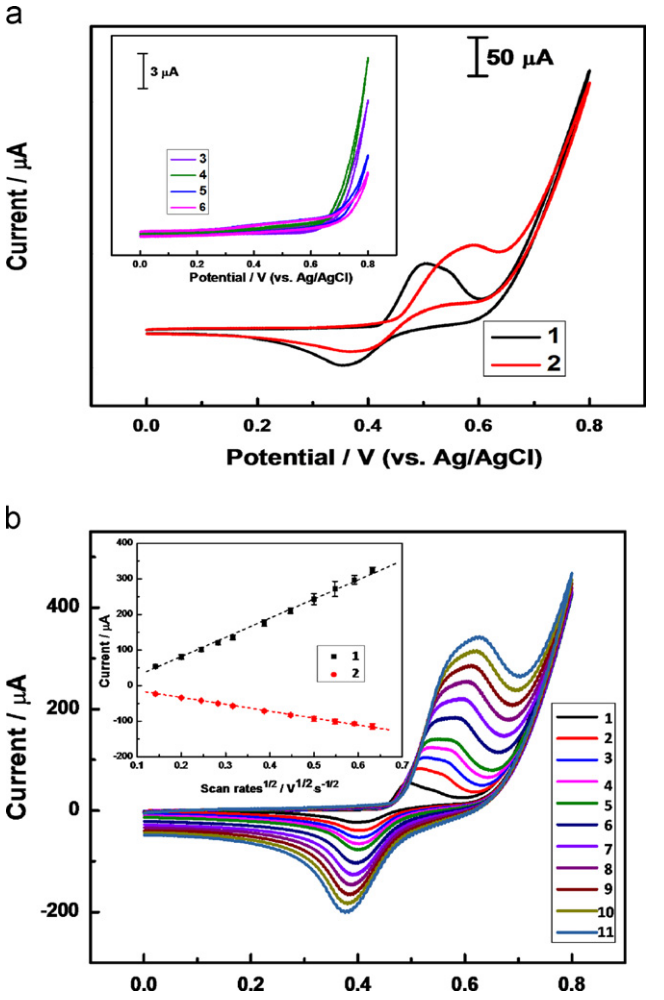

Fig. 2. (a) CVs of CS-RGO–NiNPs modified SPE in 0.1 M NaOH in the absence (1) and presence (2) of 3 mM Glc. Inset shows CVs of unmodified (3 and 4) and CS-RGO (5 and 6) modified SPEs in 0.1 M NaOH in the absence (3 and 5) or presence (4 and 6) of 5 mM Glc. Scanning from 0.0 to +0.8 V at 0.1 V s^{-1}. (b) CVs of CS-RGO–NiNPs in 0.1 M NaOH at different scan rates of 0.02, 0.04, 0.06, 0.08, 0.1, 0.15, 0.2, 0.25, 0.3, 0.35 and 0.4 V s^{-1} (inner to outer). Inset shows anodic and cathodic peak currents as a function of square root of scan rates.

$$NiO(OH) + glucose \rightarrow Ni(OH)_2 + glucolactone \quad (3)$$

In this reaction at anodic potentials, strongly oxidizing Ni(III) species oxidize Glc into glucolactone and themselves are reduced into Ni(II) species. Therefore, the concentration of Ni(III) decreases while that of Ni(II) increases, causing an increase in anodic peak current and a decrease in cathodic peak current (Lu et al., 2009). The anodic peak potential shifted to a more positive +0.60 V, possibly attributed to the diffusion-limited process of Glc at the electrode surface (Nie et al., 2011). Since the peak potential to simultaneously produce Ni(III) species and to oxidize Glc at CS-RGO–NiNPs electrode is around +0.60 V (curve 2), this potential was selected as the detection potential. The voltammetric behaviors of CS-RGO–NiNPs electrode were investigated in 0.1 M NaOH at different scan rates (Fig. 2b). As the scan rate increased from 0.02 to 0.4 V s^{-1}, both anodic and cathodic peak currents increased in proportion to the square root of scan rates. Moreover, the anodic peak potential shifted more positively while the cathodic potential shifted more negatively with increasing scan rates, thus generating a larger peak-to-peak potential separation. These results are evidence of nucleation of NiO(OH) followed by an increase in active sites in both Ni(III) and Ni(II) species (Sun et al., 2012). A

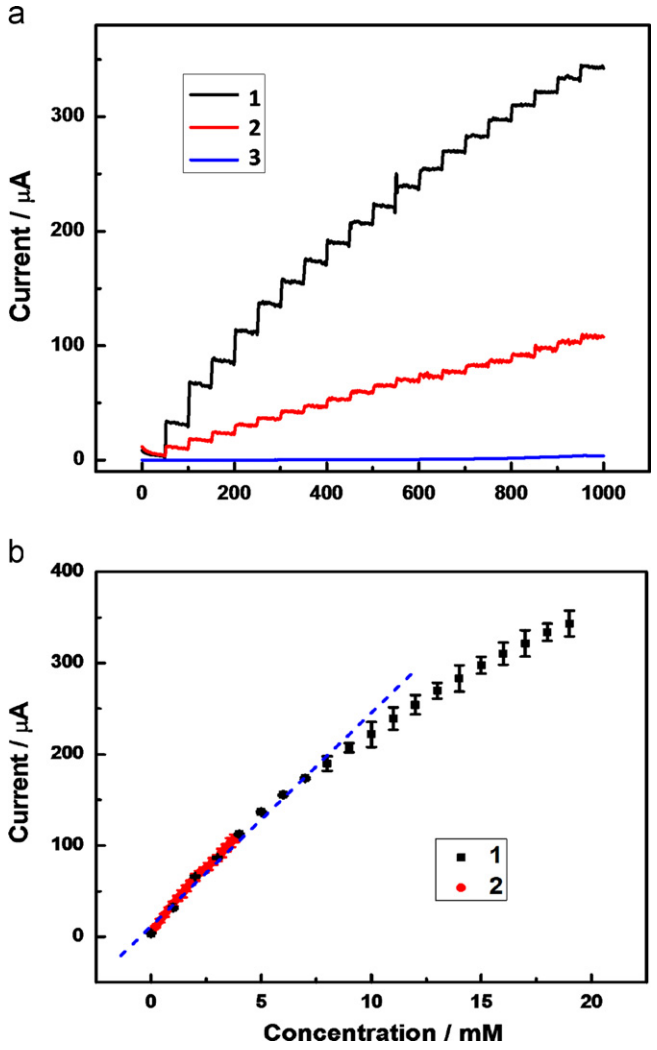

Fig. 3. (a) Amperometric responses of CS-RGO–NiNPs (1 and 2) and CS-RGO (3) SPEs in 0.1 M NaOH with stepwise addition of 1 (1 and 3) and 0.2 mM Glc (2) at 50 s intervals. (b) linearity of current response (a1 and a2) vs. Glc concentration at CS-RGO–NiNPs SPE.

linear dependence of peak currents on the square root of scan rates (Fig. 2b inset) can be established for both anodic and cathodic peak currents (R=0.999), signifying the diffusion-controlled electrochemical kinetics.

3.3. Amperometric sensing of CS-RGO–NiNPs electrode towards Glc

The amperometric responses at CS-RGO–NiNPs electrode in 0.1 M NaOH at an applied potential of +0.60 V were evaluated in Fig. 3a by dropwise successive addition of Glc in concentrations of 0.2 mM (curve 2) and 1 mM (curve 1). Consistent with CVs (Fig. 2a), CS-RGO–NiNPs electrode yielded an overwhelmingly larger current response than CS-RGO electrode (curve 3). Apparent stair-like stepwise increases in current were achieved with each addition of Glc, and steady-state currents were obtained in seconds, confirming high sensitivity and fast response. This superior performance might be owing to the high electrocatalytic activity of CS-RGO–NiNPs that offers low resistance pathways for faster electron transfer. A linear relationship was obtained between the current response and Glc concentration (I (μA)= 22.48 × C (mM)+15.29, R=0.994) from 0.2 to 9.0 mM and the two calibration curves at different concentrations almost overlapped, indicating good reproducibility and stability (Fig. 3b). The sensitivity was calculated to be 318.4 μA $mM^{-1} \cdot cm^{-2}$, and dynamic linear working range of up to 9.0 mM of Glc. The detection limit was determined to be 4.1 μM at signal/noise=3. The sensing performance of the as-prepared CS-RGO–NiNPs SPEs is compared with other reported Ni-based enzymatic or enzymeless Glc sensors in Table S2. Our sensor boasts almost the highest sensitivity, widest linear range, and excellent detection limit. Since the normal Glc level for humans is 0.1–0.8 mM in urine and 3.5–5.3 mM in whole blood (Hones et al., 2008), the wide linear range of CS-RGO–NiNPs is capable of measuring Glc at normal physiological levels either in urine or blood without diluting the samples. The Glc levels in diabetic patients are higher, and measurements may be made with appropriate dilutions.

3.4. Application of CS-RGO–NiNPs electrode in a portable microfluidic device

Electrocatalytic performance of CS-RGO–NiNPs SPEs against Glc was further studied both in a conventional electrochemical cell and in the PDMS chamber of the fabricated microfluidic device by CV using the same electrode (Fig. 4a). The electrocatalytic performance against the same concentration of Glc in the PDMS chamber of the microfluidic device was comparable to that in a stagnant conventional cell, in spite of the much smaller sample volume used in the microfluidic device. This result implies little hindrance of Glc detection from the PDMS microfluidic chamber which may actually contribute a little additional cell resistance. The selectivity of CS-RGO–NiNPs SPEs was tested in the presence of easily-oxidized compounds which are commonly coexisting with Glc in physiological samples (Fig. 4a inset). Under normal physiological conditions, the interfering species such as UA, AA and DA are present at levels lower than 0.1 mM, in other words, with Glc:interferent ratios of more than 30:1 (Park et al., 2003). However, these interferents can still produce oxidation current comparable to that of Glc, based on their higher electron transfer rates, especially at high detection potentials. Here interferents were tested at a higher ratio of 1:10 to Glc in electrochemical cell. As observed, UA nearly produced no interfering signals while slightly increases in currents were observed for AA and DA, generating 9.9% and 6.7% current changes which are not remarkable compared to the Glc current signal and are within the acceptable range. Actually, these mild current increases from interferents were previously reported in studies based on NiNPs catalysts (Nie et al., 2011) and can possibly be reduced by coating an outer molecule-selective membrane or doping Ni with other catalysts, though it might lower the sensitivity. In the meantime, the recovery rate in the presence of interferents was calculated to be 92.0%. These results suggested the sensor can be used for sensitive and specific detection of Glc virtually unaffected by the presence of common interferents.

Real-time microfluidic analysis was conducted by manually injecting a buffer solution (0.1 M NaOH) with or without Glc with a microsyringe (Fig. 4b). Samples containing either 1 mM or 0.5 mM Glc were tested, each followed by a buffer injection. Immediately after the introduction of Glc samples at the inlet, an oxidation current was generated. Though the current decayed as in electrochemical microfluidic devices due to unsteady-state diffusion (Lankelma et al., 2012), a Glc-specific current could be easily identified and diffusion-limiting current was collected. A considerable increase in current was caused initially by the high local Glc concentration on the electrode surface right after the injection (Fig. 4b inset), which was followed by the diffusion-limited process. The signal fluctuations observed is attributed to the liquid flow during each injection. Without buffer injection, there will be baseline drifts (memory effects) due to insufficient time (as in Fig. 4b inset). The average of 1 mM Glc injections was calculated to be 0.99 mM from the calibration (from single runs in the

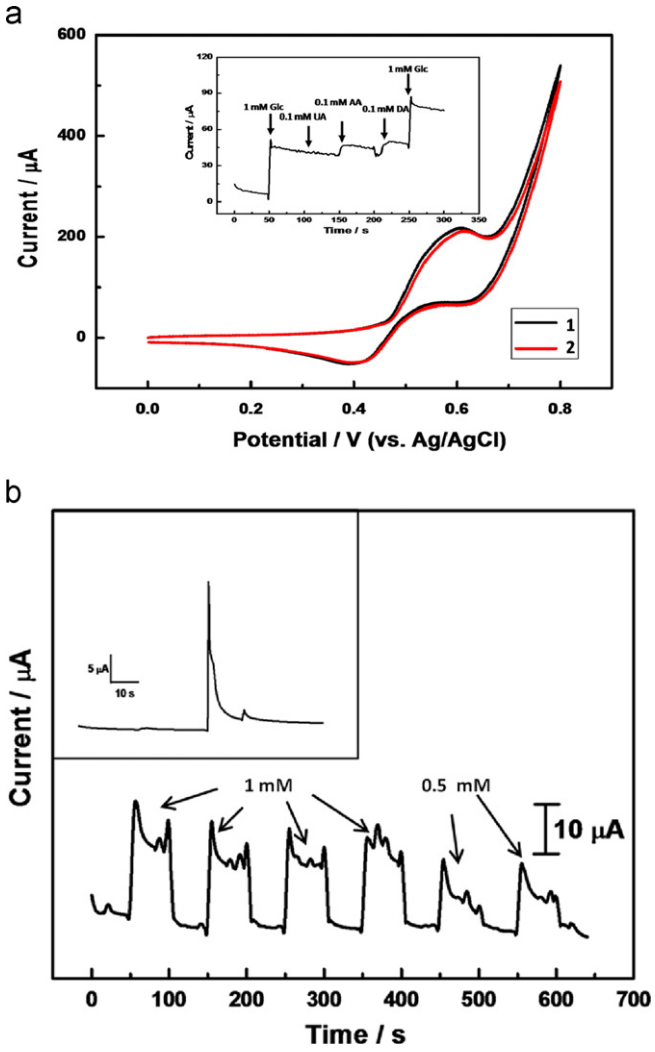

Fig. 4. (a) CVs of CS-RGO–NiNPs modified SPEs in 0.1 M NaOH containing 3 mM Glc (1) outside microfluidic chamber in a conventional electrochemical cell under unstirred conditions (2) within the PDMS microfluidic chamber. Scan rate: 0.1 V s^{-1}. Inset shows the result of sensing Glc in the presence of interferents UA, AA, and DA at an applied potential of +0.60 V. (b) Real-time amperometric detection of Glc at CS-RGO–NiNPs sensor in the microfluidic electrochemical device with successive microsyringe injections of buffer or Glc samples at 50 s intervals. Inset shows amperometric *i*–*t* curve of 0.1 mM Glc in the microfluidic device.

microfluidic device), with a relative standard deviation (RSD) of 8.7%, while 0.48 mM with RSD of 4.8% was obtained at Glc injections of 0.5 mM, demonstrating excellent accuracy in consecutive real-time Glc measurements of the electrochemical microfluidic device incorporated with disposable CS-RGO–NiNPs SPEs with minimal memory effects. Five measurements of 0.1 mM Glc by the same electrode were also tested, for which the RSD was 12.6%. In addition, five CS-RGO–NiNPs SPEs prepared under the same conditions were tested for current responses against 1 mM Glc with an RSD of 13.7%, indicating acceptable reproducibility. Stability of the sensor was investigated by measuring the sensitivity after being stored in a Petri dish under room temperature for two weeks. It still retained 84.9% of its original sensitivity. Therefore, CS-RGO–NiNPs SPEs have good stability, reproducibility and portability for Glc detection, even though they were primarily fabricated as single-use sensors.

Human urine samples were collected from healthy laboratory coworkers. Samples were diluted at a ratio of 1:2 (v/v) to 0.1 M NaOH with a final pH of 13. They were stored at 4 °C before use with no other pretreatments. Since Glc is not usually found in urine from healthy people and even if present, is in the range of 0.1–0.8 mM, standard addition method was employed to spike samples with measurable amount of standard Glc of 0.5 mM and 1 mM. Noticeably in HPLC, a retention time shift of Glc was observed from 6.5 min in water to around 6.3 min in urine samples and 6.0 min in samples diluted with NaOH. In the microfluidic analytical device, an overwhelmingly large initial current appeared after sample injection and this current quickly decayed for quantification within 15 s. As presented in Table S3, the results using electrochemical microfluidic device are close to those obtained using HPLC-amperometric detection and good recovery rates from 89 to 97% were acquired. Although no Glc could be virtually detected in subject 2 with both methods, a certain amount of Glc was surprisingly found in dense and dark yellow urine samples from healthy subject 1, approximately 0.59 mM at CS-RGO–NiNPs SPEs and 0.53 mM at HPLC. The comparatively concentrated condition of the urine sample and the Glc presence, which is still within the normal range may be caused by the dehydration or special diets of the subject when the sample was collected. These results illustrate good correspondence of the results from the analytical device to those from commercial HPLC-electrochemical instruments.

4. Conclusions

A simple, rapid, and convenient one-step approach was used to synthesize CS-RGO–NiNPs from the self-assembled nanocomposite precursor solution on SPEs, initiated simultaneously by pH-responsive electrodeposition of CS, electrochemical reduction (and deposition) of soluble GO into insoluble RGO as well as reduction of metal precursors into metal NPs. Deposited GO was electrochemically reduced *in situ* without any pre- or post-reduction steps. Uniformly distributed and interconnected NiNPs with relatively homogenous particle sizes could be observed in the CS and wrinkled ERGO scaffold. The resulting nanocomposites exhibited fast electron transfer kinetics and high electrocatalytic activity against Glc, with good sensitivity, selectivity and stability. A pocket-size, point-of-care electrochemical microfluidic sensing device was fabricated using PDMS molding and ABS plastic milling to incorporate the as-prepared disposable SPEs for real-time Glc monitoring in small sample volumes. Results of Glc measurements in human urine samples using the device correlated well with those obtained by HPLC-electrochemical instrument. The simple material synthesis, enzyme-free nature, portability, affordable cost and strong sensing performance of the reported device offers out-of-lab and beaker-free Glc sensing in healthcare.

Acknowledgments

The authors are thankful to funding support to JY through Hjalmar D. and Janet W. Bruhn Fellowship and Louis and Elsa Thomsen Wisconsin Distinguished Graduate Fellowship provided at UW-Madison.

Appendix A. Supporting information

Supplementary data associated with this article can be found in the online version at http://dx.doi.org/10.1016/j.bios.2013.03.051.

References

Adewuyi, S., Kareem, K.T., Atayese, A.O., Amolegbe, S.A., Akinremi, C.A., 2011. International Journal of Biological Macromolecules 48, 301–303.

Ai, H., Huang, X., Zhu, Z., Liu, J., Chi, Q., Li, Y., Li, Z., Ji, X., 2008. Biosensors and Bioelectronics 24, 1048–1052.
Bulwan, M., Zapotoczny, S., Nowakowska, M., 2009. Soft Matter 5, 4726–4732.
Chen, Y., Zhang, X.O., Zhang, D.C., Yu, P., Ma, Y.W., 2011. Carbon 49, 573–580.
Han, D., Han, T., Shan, C., Ivaska, A., Niu, L., 2010. Electroanalysis 22, 2001–2008.
Hones, J., Muller, P., Surridge, N, 2008. Diabetes Technology & Therapeutics 10, S10–S26.
Huang, H.-Y., Chen, P.-Y., 2010. Talanta 83, 379–385.
Jawaheer, S., White, S.F., Rughooputh, S.D.D.V., Cullen, D.C., 2003. Biosensors and Bioelectronics 18, 1429–1437.
Joo, S., Park, S., Chung, T.D., Kim, H.C., 2007. Analytical Sciences 23, 277–281.
Kadara, R.O., Jenkinson, N., Banks, C.E., 2009. Sensors and Actuators B: Chemical 138, 556–562.
Lankelma, J., Nie, Z., Carrilho, E., Whitesides, G.M., 2012. Analytical Chemistry 84, 4147–4152.
Liu, C.B., Wang, K., Luo, S.L., Tang, Y.H., Chen, L.Y., 2011. Small 7, 1203–1206.
Lu, L.M., Zhang, L., Qu, F.L., Lu, H.X., Zhang, X.B., Wu, Z.S., Huan, S.Y., Wang, Q.A., Shen, G.L., Yu, R.Q., 2009. Biosensors and Bioelectronics 25, 218–223.
Luo, L., Li, Q., Xu, Y., Ding, Y., Wang, X., Deng, D., Xu, Y., 2010. Sensors and Actuators B: Chemical 145, 293–298.
Luo, P.F.F., Kuwana, T., Paul, D.K., Sherwood, P.M.A., 1996. Analytical Biochemistry 68, 3330–3337.
Luo, X.L., Xu, J.J., Du, Y., Chen, H.Y., 2004. Analytical Biochemistry 334, 284–289.
Maalouf, R., Chebib, H., Saikali, Y., Vittori, O., Sigaud, M., Jaffrezic-Renault, N., 2007. Biosensors and Bioelectronics 22, 2682–2688.
Martis, P., Dilimon, V.S., Delhalle, J., Mekhalif, Z., 2010. Electrochimica Acta 55, 5407–5410.
Mu, Y., Jia, D., He, Y., Miao, Y., Wu, H.-L., 2011. Biosensors and Bioelectronics 26, 2948–2952.
Nasirpouri, F., Bending, S.J., Peter, L.M., Fangohr, H., 2011. Thin Solid Films 519, 8320–8325.
Nie, H., Yao, Z., Zhou, X., Yang, Z., Huang, S., 2011. Biosensors and Bioelectronics 30, 28–34.
Park, I., Cheng, J., Pisano, A.P., Lee, E.S., Jeong, J.H., 2007. Applied Physics Letters, 90.
Park, S., Chung, T.D., Kim, H.C., 2003. Analytical Chemistry 75, 3046–3049.
Pei, S., Zhao, J., Du, J., Ren, W., Cheng, H.-M., 2010. Carbon 48, 4466–4474.
Potara, M., Baia, M., Farcau, C., Astilean, S., 2012. Nanotechnology, 23.
Rohlfing, C.L., Wiedmeyer, H.-M., Little, R.R., England, J.D., Tennill, A., Goldstein, D.E., 2002. Diabetes Care 25, 275–278.
Segal, M., 2009. Nature Nanotechnology 4, 612–614.
Sun, A., Zheng, J., Sheng, Q., 2012. Electrochimica Acta 65, 64–69.
Toghill, K.E., Xiao, L., Phillips, M.A., Compton, R.G., 2010. Sensors and Actuators B: Chemical 147, 642–652.
Vlandas, A., Kurkina, T., Ahmad, A., Kern, K., Balasubramanian, K., 2010. Analytical Chemistry 82, 6090–6097.
Wan, Y., Lin, Z., Zhang, D., Wang, Y., Hou, B., 2011. Biosensors and Bioelectronics 26, 1959–1964.
Wang, J., Thomas, D.F., Chen, A., 2008. Analytical Chemistry 80, 997–1004.
Wei, D., Qian, W., 2008. Colloids and Surfaces B: Biointerfaces 62, 136–142.
Wu, L.-Q., Lee, K., Wang, X., English, D.S., Losert, W., Payne, G.F., 2005. Langmuir 21, 3641–3646.
Yang, J., Deng, S.Y., Lei, J.P., Ju, H.X., Gunasekaran, S., 2011a. Biosensors and Bioelectronics 29, 159–166.
Yang, J., Strickler, J.R., Gunasekaran, S., 2012. Nanoscale 4, 4594–4602.
Yang, L., Xiong, H., Zhang, X., Wang, S., Zhang, X., 2011b. Biosensors and Bioelectronics 26, 3801–3805.
Yang, S., Liu, X., Zeng, X., Xia, B., Gu, J., Luo, S., Mai, N., Wei, W., 2010. Sensors and Actuators B: Chemical 145, 762–768.
Zeng, X., Li, X., Xing, L., Liu, X., Luo, S., Wei, W., Kong, B., Li, Y., 2009. Biosensors and Bioelectronics 24, 2898–2903.
Zhao, C., Shao, C., Li, M., Jiao, K., 2007. Talanta 71, 1769–1773.